Photoacoustics 26 (2022) 100344

Contents lists available at ScienceDirect

Photoacoustics

journal homepage: www.elsevier.com/locate/pacs

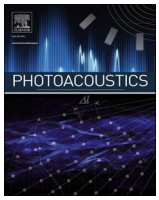

Myocardial infarct border demarcation by dual-wavelength photoacoustic spectral analysis

Kangmu Ma [a,1], Shiying Wu [b,c,1], Shixing Huang [a], Weiya Xie [b,c], Mengjiao Zhang [b,c], Yingna Chen [b,c], Pengxiong Zhu [a], Jun Liu [d,*], Qian Cheng [b,c,*]

[a] Department of Cardiovascular Surgery, Ruijin Hospital, Shanghai Jiao Tong University School of Medicine, Shanghai, China
[b] Institute of Acoustics, School of Physics Science and Engineering, Tongji University, Shanghai, China
[c] MOE Frontiers Science Center for Intelligent Autonomous Systems, Tongji University, Shanghai, China
[d] Department of Cardiac Surgery, East Hospital, Tongji University School of Medicine, Shanghai, China

ARTICLE INFO

Keywords:
Myocardial infarct border demarcation
Dual-wavelength photoacoustic measurement
Photoacoustic spectral analysis
Specific molecular content determination

ABSTRACT

Myocardial infarction (MI) is a major cause of morbidity and mortality worldwide. Modern therapeutic strategies targeting the infarct border area have been shown to benefit overall cardiac function after MI. However, there is no non-invasive diagnostic technique to precisely demarcate the MI boundary till to now. In this study, the feasibility of demarcating the MI border using dual-wavelength photoacoustic spectral analysis (DWPASA) was investigated. To quantify specific molecular characteristics before and after MI, "the ratio of the areas of the power spectral densities (R_{APSD})" was computed from the DWPASA results. Compared to the normal tissue, MI tissue was shown to contain more collagen, resulting in higher R_{APSD} values ($p < 0.001$). Cross-sectional MI lengths and the MI area border demarcated in two dimensions by DWPASA were in substantial agreement with Masson staining (ICC = 0.76, $p < 0.001$, IoU = 0.72). R_{APSD} has been proved that can be used as an indicator of disease evolution to distinguish normal and pathological tissues. These findings indicate that the DWPASA method may offer a new diagnostic solution for determining MI borders.

1. Introduction

Myocardial infarction (MI) is a major cause of morbidity and mortality worldwide [1]. Percutaneous coronary intervention or cardiac bypass surgery to implement revascularization combined with standard medical treatments are common clinical strategies for MI. Those who survive acute MI often suffer from progressive left ventricular systolic function impairment, in which case congestive heart failure is inevitable. Such patients represent a heavy social burden for modern health care services [2]. The preservation or regeneration of cardiomyocytes, an attempt to reverse negative aspects of the process of MI-induced necrosis, has not been definitively achieved [3]. Modern therapeutics—including stem cell, biomaterial, gene, and growth hormone therapies—targeting the infarct border have been shown to benefit overall cardiac function by retaining and restoring contractile properties after MI [4]. Conventional clinical imaging techniques have been used to evaluate the borders of infarctions. However, these imaging modalities have limitations. Ultrasound (US) has poor contrast in soft tissues [5]. Single-photon emission computed tomography (SPECT) and positron emission tomography (PET) suffer from relatively low spatial resolution [6] and magnetic resonance imaging (MRI) is time consuming [7]. Developing an real-time and non-invasive imaging technique that can effectively demarcate the MI border is of paramount importance.

Biomedical photoacoustic (PA) imaging is an emerging technique combining excellent optical absorption contrast, high ultrasonic resolution, and relatively deep penetration depth (up to a few cm) that has been explored widely over the past decade for the diagnosis of many diseases [8–19]. The accurate assessment of physical or chemical differences in tissues, such as collagen and lipid composition variation or hemoglobin oxygenation status changes, is a unique advantage of PA imaging. This technique can be used to obtain a comprehensive picture at both the microscopic and macroscopic levels of human and animal tissue. In previous studies, using the absorption peak of hemoglobin at 800 nm, Liming Nie et al. demonstrated the capacity of PA imaging to noninvasively localize and characterize MI in vivo. Their results revealed that the occurrence of MI led to a decrease in the intensity of

* Corresponding authors at: Institute of Acoustics, School of Physics Science and Engineering, Tongji University, Shanghai, China
E-mail addresses: liujun52@126.com (J. Liu), q.cheng@tongji.edu.cn (Q. Cheng).
[1] † These authors contributed equally to this paper.

https://doi.org/10.1016/j.pacs.2022.100344
Received 2 November 2021; Received in revised form 3 March 2022; Accepted 4 March 2022
Available online 5 March 2022

hemoglobin PA signals, and using linear regression they observed good proportional correlation between results obtained via PA and conventional triphenyl tetrazolium chloride (TTC) staining methods, for the injured MI area and entire lesion site over time [20]. Multiple wavelengths photoacoustic technology can achieve the aim that quantitatively measuring the change of biomacromolecule chemical components and physiological indicators. Now, multiple wavelengths PA imaging have widely been used in many diseases. For example, Wood et al. used an optimized PA imaging technique to assess the oxygen saturation in the bone marrow cavity during disease progression in a murine model of acute lymphoblastic leukemia, based on the wavelengths of 715, 730, 760, 800, 850, and 880 nm [22]. In addition, multiple wavelength PA imaging also can be used in the detection of inflammation and fibrosis associated with Crohn's disease [23], and for evaluation of the condition of the liver [24]. Our group has also used the multi-wavelength analysis PA method to extract the relative collagen content values, PA physicochemical analysis-quantified parameters so as to evaluate the osteoporosis progression [25,26]. At present, multi-wavelengths PA spectrum analysis technique has been widely used in many disease detection. However, in the field of heart disease research, PA studies have manly been focused on the measurement of changes in morphology and hemoglobin function, or involved the use of exogenous contrast agents to distinguish cardiovascular lesions in ischemic heart disease. However, it is well known that the expansion of activated fibroblasts into the infarcted myocardium, initiation of the fibrotic response, and collagen deposition are prominent features after MI [27], that is, molecular changes are known to occur after MI. Hence, the potential of PA to produce image contrast based on molecular differences within injured tissue inspired us to attempt to develop a new PA-based modality to demarcate the MI border by observing collagen content variation after MI.

This study aimed to validate the feasibility of dual-wavelength PA spectral analysis (DWPASA) to quantify specific molecular characteristics associated with MI to achieve MI border demarcation. *Ex vivo* PA experiments were conducted using samples of a rat MI model. Based on a frequency-domain analysis of broadband PA signals obtained via excitation at two wavelengths, namely 1310 and 1450 nm, a quantitative DWPASA parameter, "the ratio of the areas of the power spectral densities (R_{APSD})" was defined to quantify specific molecular characteristics before and after MI. The reliability of this novel method was assessed by comparing MI cross-sectional lengths and two-dimensional projections of MI shapes (areas) obtained using the DWPASA method with those determined using standard Masson staining. In this study, R_{APSD} has been proved that is much more sensitive to the disease evolution than PA signal amplitude of individual molecules, and thus can be used as an indicator of disease evolution to distinguish normal and pathological tissues.

2. Methods

2.1. Animal model

This study complied with the standards for the care and use of laboratory animals of the National Institute of Health Laboratory Animal Center (China). Ten Sprague–Dawley (SD) rats were used in the study. All experiments were approved by the Animal Research Ethical Committee of Shanghai Jiao Tong University and were conducted with adherence to approved guidelines and regulations. Adult male SD rats weighing 230–250 g (from the Laboratory Animal Care Facility of Shanghai Jiao Tong University School of Medicine) were used to construct MI models and were housed at a constant temperature ($22 \pm 2\,^{\circ}C$) under a 12-h light–dark cycle and given access to standard laboratory chow and water ad libitum. The MI model was constructed as previously described [22]. Briefly, animals were anesthetized by 2% isoflurane inhalation, intubated, and ventilated using a respirator with extra oxygen. The rat chests were shaved, sterilized with povidone–iodine solution, and opened via left thoracotomy at the 4th intercostal space. As shown in Fig. 1(a) and (b), the pericardium was removed, and the left anterior descending (LAD) coronary artery was permanently ligated with a suture (5–0 PROLENE, Ethicon) to induce MI. The chests were then closed and sutured. Animals 7- and 14-days post-MI were used for the study. A flowchart of the complete experiment is shown in Fig. 1(c). Fig. 1(d) and 1(e) compare examples of the infarct lengths obtained via Masson staining and DWPASA, respectively. When measuring the cross-sectional Masson staining length of a slice, the slice was oriented in the same direction as the DWPASA image to ensure that the comparison between the two methods was accurate. Within a specific projected segment, one or more Masson positive subsections are typically present (Fig. 1(d)). We segmented the subsections manually. Hence, the cross-sectional length of a slice is the cumulative of length of all the positive subsections (Masson staining cumulative length, CL_M). Similarly, in the DWPASA analysis, the cross-sectional length of the slice is defined as the cumulative of lengths of the subsections, and this we term the DWPASA cumulative length, CL_{DWPASA}. From Fig. 1(e), as an example, the lengths of the stained pixels (object or foreground pixels) in a single line in the x direction in the PA scanning planes are summed to obtain a CL_{DWPASA} value. In this plot, the origin is the intersection of the left edge and the apex of the heart; the x axis coordinate indicates the distance to the left edge of the heart, and the y axis coordinate denotes the distance to the apex of the heart. The infarct length at the Apex + 6 mm position, for example, is the sum of two subsections with lengths of 3 and 6 mm, respectively, (Fig. 1(e)).

2.2. Dual-wavelength PA spectral analysis theory

PA signals can reveal information about specific molecular characteristics, such as details of the biomacromolecule content of tissue. When a sample is irradiated with two specific wavelengths, the PA signals generated will include the main biomacromolecule absorption characteristics at the corresponding wavelengths. The PA signal amplitude generated by the sample under ideal conditions can be expressed as [28–30]:

$$p(t,\lambda) = k \bullet \Gamma \bullet \eta_{th} \bullet \mu_a(\lambda) \bullet I_0 \bullet e^{-\alpha_s \bullet d}, \tag{1}$$

where Γ is the Grüneisen parameter ($\Gamma = \frac{\beta \bullet c^2}{C_p}$ with β being the thermal coefficient of volume expansion, c is the speed of sound in tissue, and C_p is the heat capacity at constant pressure); k is a constant accounting for the impulse response of the detection system; η_{th} is the heat conversion efficiency; I_0 is the light fluence generated by the laser; α_s is the ultrasound attenuation coefficient in the sample; and d is the thickness of the sample. For the same sample,Γ, k, η_{th}, I_0, and α_s can be considered to be approximately equal at the two different wavelengths. $\mu_a(\lambda)$ is the total optical absorption coefficient of the sample at the wavelength of λ, which is the content weighted average of the optical absorption coefficient of various molecules in the sample as shown in Eq. (2).

$$\mu_a(\lambda) = C_1 \bullet \mu_1(\lambda) + C_2 \bullet \mu_2(\lambda) + \ldots + C_n \bullet \mu_n(\lambda) \tag{2}$$

Here C_i and $\mu_i(\lambda)(i = 1, 2, \ldots n)$ are the content percentages and their optical absorption coefficient of different molecules in the sample, respectively. If molecule A increases while molecule B decreases in biological tissue during disease evolution, and A and B dominate the light absorption coefficients at certain wavelengths, A and B can be regarded as biomarkers of pathological and normal tissues, respectively, e.g. the collagen for MI at 1310 nm or the water for normal tissue at 1450 nm. Hence, the ratio of their PA signal amplitude can be simplified as:

$$R = \frac{p(t,\lambda_A)}{p(t,\lambda_B)} = \frac{k \bullet \Gamma \bullet \eta_{th} \bullet \mu_a(\lambda_A) \bullet I_0 \bullet e^{-\alpha_s \bullet d}}{k \bullet \Gamma \bullet \eta_{th} \bullet \mu_a(\lambda_B) \bullet I_0 \bullet e^{-\alpha_s \bullet d}} = \frac{\mu_a(\lambda_A)}{\mu_a(\lambda_B)} \cong \frac{C_A \bullet \mu_A(\lambda)}{C_B \bullet \mu_B(\lambda)} \propto \frac{C_A}{C_B}, \tag{3}$$

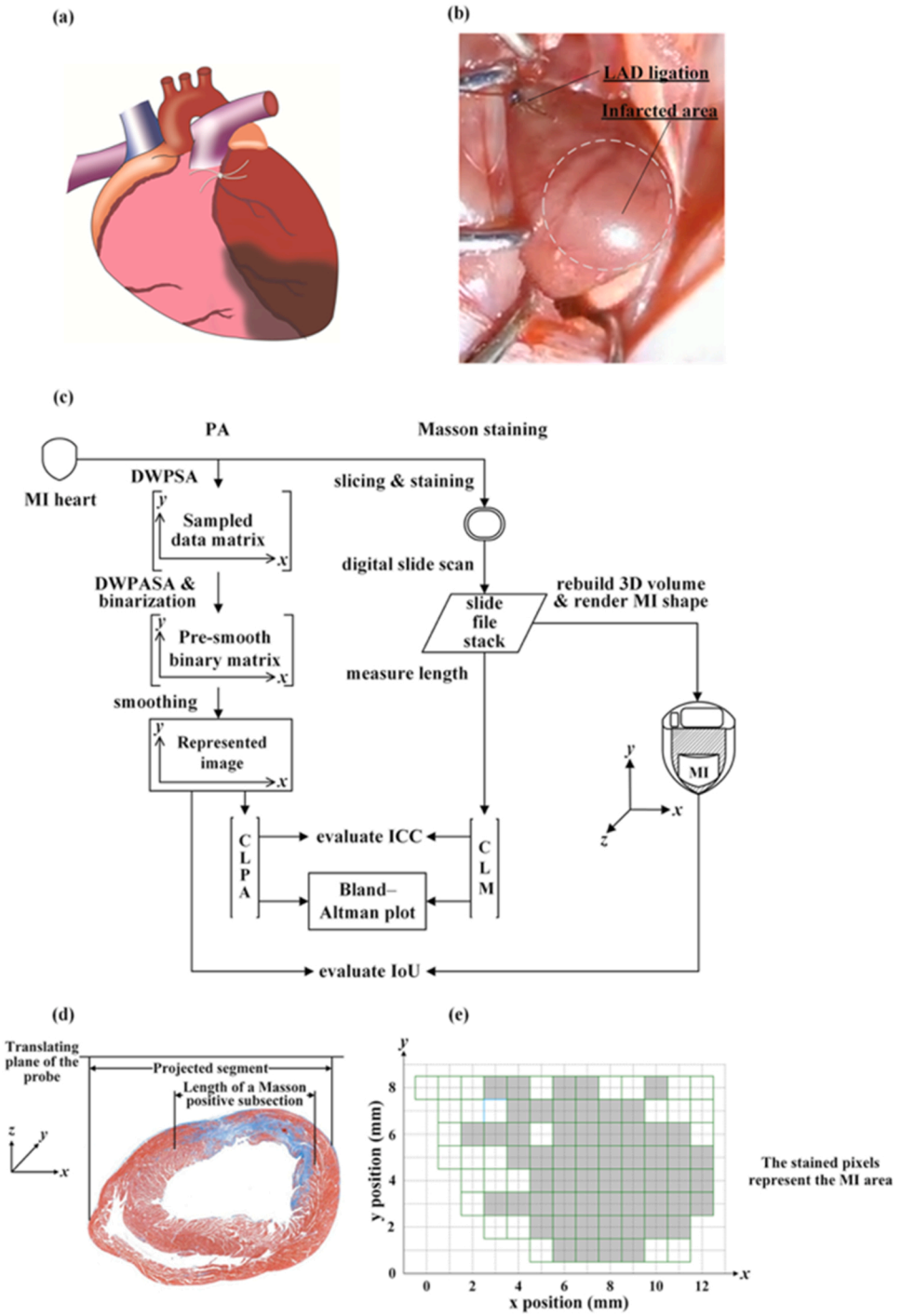

Fig. 1. Rat model of myocardial infarction and experiment flowchart. (a) Anatomical scheme of a mouse heart with MI. (b) Photograph of a rat heart after ligation of left anterior descending (LAD) coronary artery as a model for MI. (c) Flowchart showing experimental procedures of the study. (d), (e) Illustration of infarct length calculation: (d) Masson staining cumulative length (CL_M) and (e) DWPASA cumulative length (CL_{DWPASA}). Key: DWPASA, dual-wavelength photoacoustic spectral analysis; DWPSA, dual-wavelength photoacoustic signal acquisition; ICC, intraclass correlation coefficient (two-way random, absolute agreement); IoU, Intersection over Union—also known as Jaccard index—the most commonly used metric for comparing the similarity between two arbitrary shapes.

Where, the symbol "∝" means "be proportional to". Eq. (3) shows that R is proportional to the ratio of their contents. Due to the trade-off between A and B, R is much more sensitive to the disease evolution than PA signal amplitude of individual molecules, and thus can be used as an indicator of disease evolution to distinguish normal and pathological tissues.

However, in actual measurements, $p(t,\lambda)$ is affected by the bandwidth of the hydrophone, low-frequency system noise and high-frequency measurement noise. In order to minimize the effects of noise, we propose a quantitative parameter "the ratio of the areas of the power spectral density R_{APSD}" based on the PA spectral analysis to filter the noise, as shown in Eq. (4),

$$R_{APSD} = \frac{\int_{f_0}^{f_1} p^2(f,\lambda_A)\mathrm{d}f}{\int_{f_0}^{f_1} p^2(f,\lambda_B)\mathrm{d}f} = \frac{\mu_a^2(\lambda_A)}{\mu_a^2(\lambda_B)} \cong \frac{C_A^2}{C_B^2}\frac{\mu_A^2(\lambda)}{\mu_B^2(\lambda)} \propto \frac{C_B^2}{C_B^2} \tag{4}$$

Here, $p(f,\lambda)$ is the Fourier transform of $p(t,\lambda)$; $p^2(f,\lambda)$ is the power spectral density; f_1 and f_0 are the integral upper and lower limits for the integration of the power spectral density area respectively, are selecting by taking into account the influence of the hydrophone bandwidth, system noise, detection noise and high-frequency energy attenuation; $\int_{f_0}^{f_1} p^2(f,\lambda)\mathrm{d}f$ means the PA signal energy between f_0 and f_1. Therefore, R_{APSD} accurately and sensitively reflects changes in PA biomarkers during the evolution of disease, and has the ability to

distinguish diseased tissues from normal tissues.

2.3. PA experimental setup

Ten Sprague–Dawley (SD) rats were used in the study, as shown in Fig. 2(a). Each sample was observed using multiple wavelengths spanning 1200–1800 nm with a constant interval of 10 nm (in total, 60 wavelengths). A schematic of the experimental setup is shown in Fig. 2 (b). A laser light beam with a 10-Hz repetition rate and a pulse width of 2–5 ns was generated for each wavelength using a tunable optical parametric oscillator (OPO; Phocus Mobile, OPOTEK, Carlsbad, CA). The laser energy density at the sample was approximately 0.75 mJ/cm^2, which is lower than the safety limit recommended by the American National Standards Institute (ANSI). To account for variations in the laser energy, 10% of the laser beam was guided to a blackbody through a beam splitter. The blackbody signal was received by a 1 MHz ultrasonic transducer (V302, Immersion Transducers, Olympus Corp., Tokyo, Japan) immersed in a water tank to calibrate the laser energy.

As shown in Fig. 3(a), a prototype needle probe was fabricated for signal acquisition. This consisted of a needle hydrophone with a bandwidth of 1–20 MHz (HNC1500, ONDA Corp., Sunnyvale, CA) attached to a water capsule designed to couple PA signals and avoid the generation of interfering PA signals by water illumination. PA signals acquired by the hydrophone were amplified using a low-noise amplifier (5072PR, Olympus Corp., Tokyo, Japan) and recorded by a digital oscilloscope (HDO6000, Teledyne Lecroy, USA) at a sampling rate of 2500 MHz. To demarcate the MI border, we performed point-by-point scanning of the infarcted heart surfaces of ten male rats using raster scanning mode; the scanning path is shown in Fig. 3(b).

2.4. PA signal processing

All PA signal processing was performed using the MATLAB software (MATLAB R2018a). To demarcate the MI border of each sample, the following steps were used. Step 1: We first selected the two specific excitation wavelength bands for which the difference in signal between the normal and MI tissue was greatest. Step 2: Point-by-point scanning, with a step size of 1 mm, was performed for each sample at the two wavelengths, as shown in Fig. 3(b). Step 3: The amplitude of the PA signal acquired from each point at each wavelength was divided by the amplitude of the simultaneously acquired calibration PA signal from the blackbody. A typical normalized time-domain signal is plotted in Fig. 4 (a). Step 4: The PA signal was transferred to the frequency domain using Welch's method with a 4-μs moving Hamming window and an overlap of 60%, as shown in Fig. 4(b). Step 5: The parameter R_{APSD} was quantified for each spatial point. To do this, we integrated over the acoustic frequency range of 1–10 MHz. The value of 1 MHz was selected for the lower-frequency limit to avoid strong low-frequency noise. For the upper-frequency limit, 10 MHz corresponded to the value at which the maximum spectral density dropped by 20 dB. Step 6: Steps 2–5 were repeated for the PA signals from the infarcted surface of each MI model sample. Step 7: The threshold was set. In this study, to determine an expression for the optimal threshold, we used a trial-and-error method on 10 MI-mode samples (7-days post-MI for 5 samples and 14-days post-MI for 5 samples, a total of 71 MI slices were included) to obtain an expression corresponding to the PA results being as similar as possible to the Masson staining results (the gold standard), as shown in the Table A1 (Appendix File 1). The obtained threshold expression was as follows:

$$R_{\text{threshold}} = \frac{R_{\text{APSD}_{\max}} - R_{\text{APSD}_{\min}}}{2} + R_{\text{APSD}_{\min}} \quad (4)$$

Here, $R_{APSDmax}$ and $R_{APSDmin}$ refer to the maximum and minimum R_{APSD} values, respectively, for each sample. Therefore, for each sample, the value of $R_{threshold}$ was different because of individual differences among the samples. Step 8: The MI border was demarcated for each sample. Points at which the R_{APSD} value was greater than $R_{threshold}$ were considered infarcted; otherwise, the point was considered to be located in a region of normal tissue. Step 9: A smoothing protocol (detailed in Appendix File 2) was used to optimize the DWPASA results.

2.5. Rendering MI zone shape from histological slice images

Using the 3D visual software Amira 5.4.3 (Visualization Sciences Group, SAS), we projected the shapes of the MI zone onto ventricular walls reconstructed from histological slice images via the following procedure. Imported histological slice image files stack was aligned to make a consistent stack of images. Then the color images were converted into red monochromatic images. The images were then segmented into infarcted and non-infarcted areas via thresholding on the intensity of the Masson staining, and the corresponding 3D volume was reconstructed. Using the same orientation as in the DWPASA method, we clipped off the front non-infarcted volume to expose a 2D cross section containing infarcted area in the 3D rendered volume, leaving the other non-infarcted areas intact. The MI zone shape obtained via thresholding was projected onto the reconstructed 3D heart (Fig. 5).

2.6. Statistical analysis

2.6.1. ICC

Intraclass correlation coefficient (ICC) estimates and their 95% confidence intervals (CI) were calculated based on a single rater,

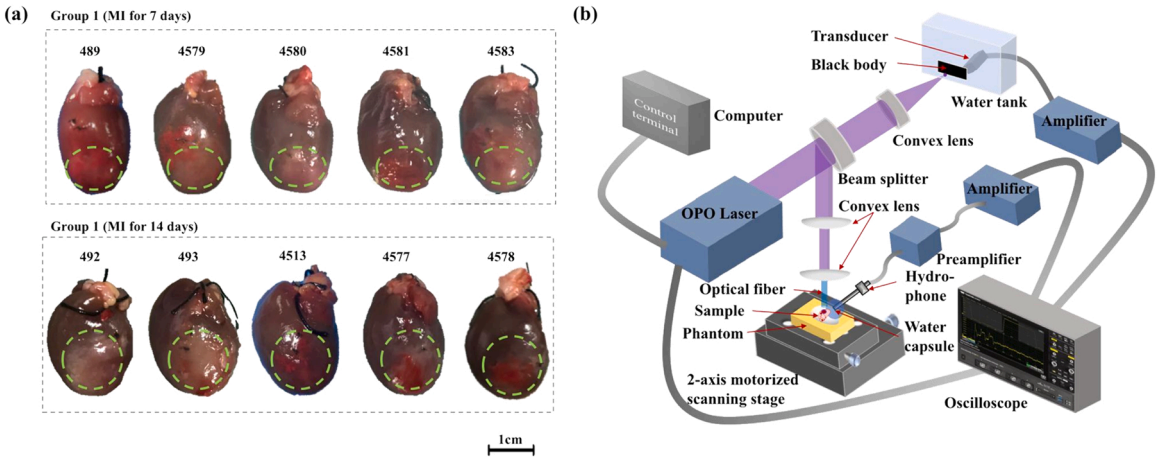

Fig. 2. Myocardial infarction (MI) rat hearts and PA setup. (a) Photos of MI model tissue (the overlaid green dashed line indicates the extent of each MI area). (b) Experimental setup for PA measurement. (For interpretation of the references to colour in this figure legend, the reader is referred to the web version of this article.)

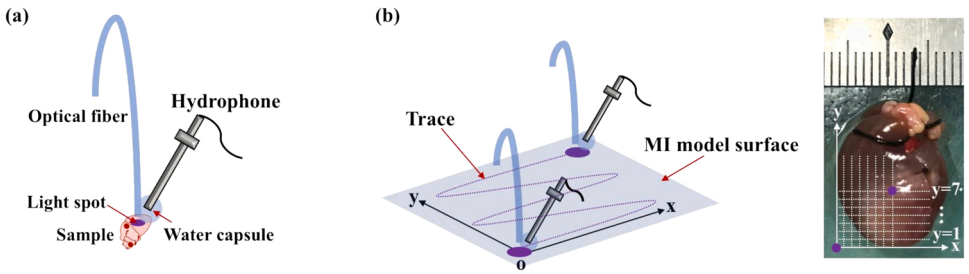

Fig. 3. Photoacoustic (PA) needle probe and image acquisition scheme. (a) Prototype PA needle probe. (b) Schematic of point-by-point signal acquisition path (left) with point-scan coordinates illustrated on a photograph of the heart (right).

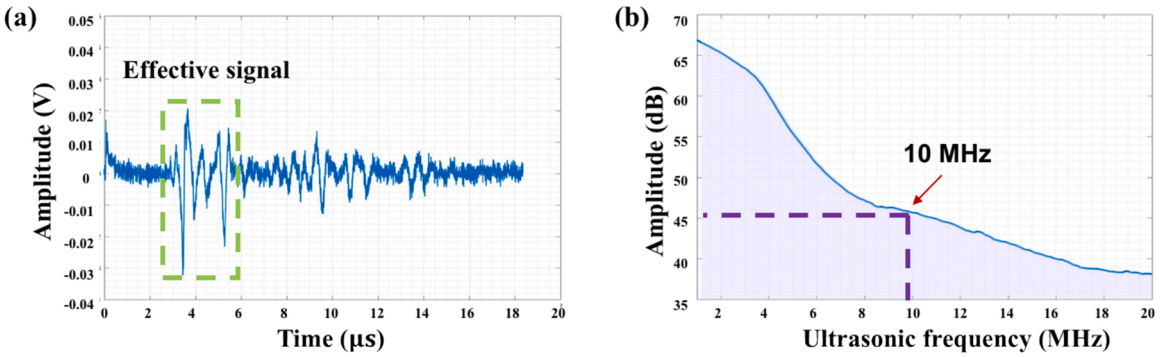

Fig. 4. PA signal processing. (a) Representative PA signal generated by tissue sample. The box with the green dashed outlined box indicates the effective signal length. (b) Typical PA frequency power spectral density generated by sample tissue. (For interpretation of the references to colour in this figure legend, the reader is referred to the web version of this article.)

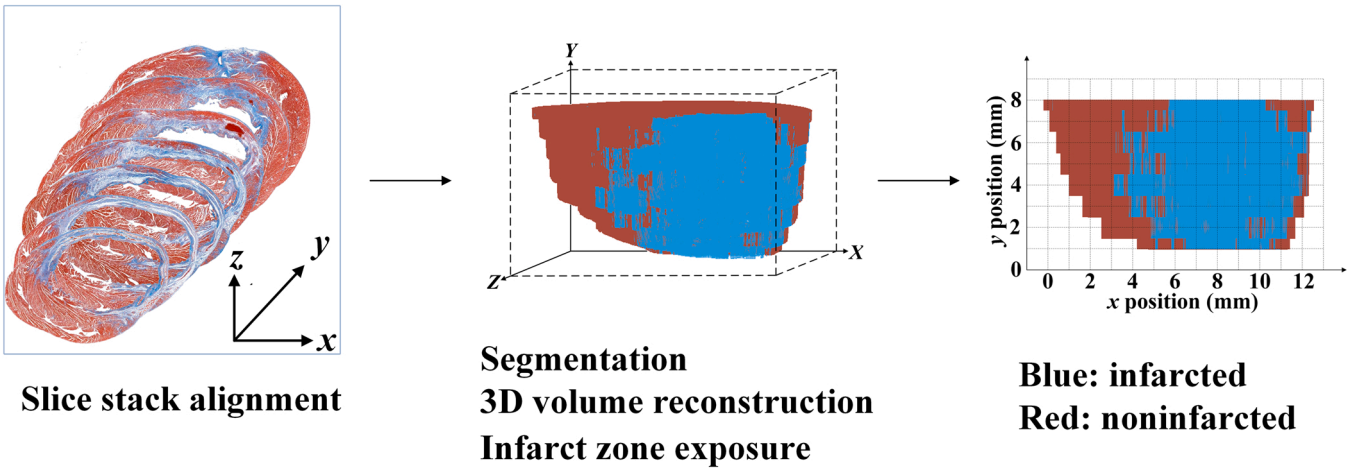

Fig. 5. Rendering the MI zone shape from histological slice images.

absolute-agreement, two-way random-effects model. ICCs were classified by means of the method suggested by Landis and Koch: 0–0.20 = "slight," 0.21–0.40 = "fair," 0.41–0.60 = "moderate," 0.61–0.80 = "substantial," and 0.81–1.00 = "(almost) perfect" [31,32]. The ICC calculations were performed using the SPSS statistical package (version 22; IBM Corporation, Armonk, NY). Statistical significance was set at $p < 0.05$.

2.6.2. Bland–altman plot

Bland–Altman (B–A) plots showing difference vs. average for the sectional infarct lengths as measured by PA analysis and Masson staining, with 95% limits of agreement (LOA), were made using Prism 6 (GraphPad Software, Inc., La Jolla, CA).

3. Results

3.1. Physio-chemical spectrogram of normal and infarcted myocardial tissues

As shown in Fig. 6(a) and 6(b), the obtained physio-chemical spectrograms indicate remarkable differences between the infarcted and normal tissues. The physio-chemical spectrogram was obtained by combining the power spectra of the PA signals obtained in the wavelength range from 1200 to 1800 nm, as detailed in our previous work [18,19].

In the physio-chemical spectrograms, optical wavelength, representing the relative optical absorption of different molecular components, is plotted on the horizontal axis, and ultrasonic frequency, from

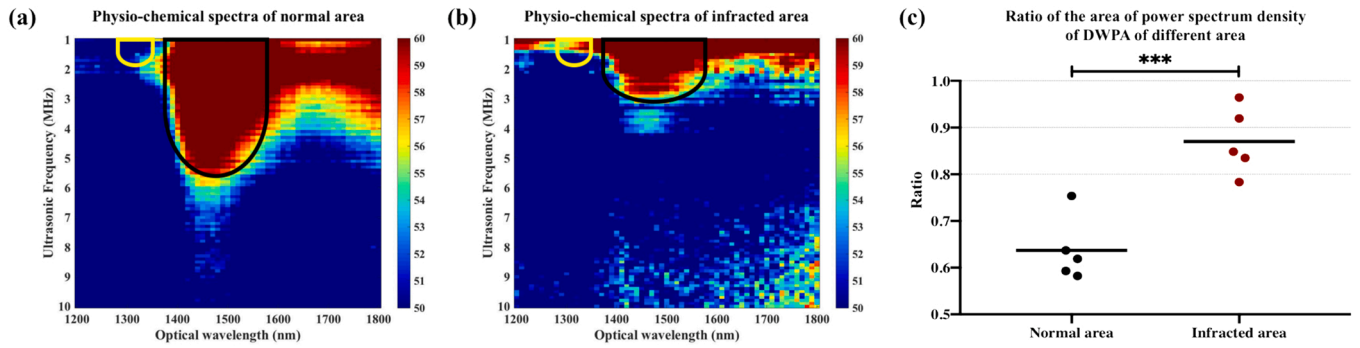

Fig. 6. Physio-chemical spectrograms of (a) normal and (b) infarcted tissues. (c) R_{APSD} statistics, which can be used to differentiate between normal and infarcted tissues. (***statistically significant difference via *t*-test($p < 0.001$), *t*-test was conducted using GraphPad Prism 9.0).

which the size distribution of the molecular clusters can be obtained, is plotted on the vertical axis; the color indicates the amplitude of the power spectral density. It is well known that collagen deposition is a prominent feature after MI [21], that is, molecular content changes are known to occur after MI. Therefore, the optical absorption characteristics are much more information-rich than the acoustic frequency response.

Compared to the physio-chemical spectrograms of the normal tissue, at 1310 nm, the MI tissue spectrograms have greater spectral magnitudes, suggesting a higher collagen content [18,19,33,34], as indicated by the yellow contours in Fig. 6(a) and (b). By contrast, at 1450 nm, the physio-chemical spectrograms of MI tissue have lower spectral magnitudes in the frequency range of 1–10 MHz than the physio-chemical spectrograms of the normal tissue, suggesting a lower water content [18,19,33,34] as indicated by the black contours in Fig. 6(a) and (b). Given the known pathological changes that occur because of MI, specifically, the replacement of cardiac muscle by scar tissue [35], an increase in collagen and a decrease in water at the lesion site were expected to be manifested at the optical wavelengths of 1310 and 1450 nm, respectively. Furthermore, we extracted the ratio parameter R_{APSD} for 1310 and 1450 nm to quantify changes in these chemical components of the tissue: the higher the ratio, the higher the collagen content and the lower the water content. To verify the reliability of R_{APSD} as a biomarker of MI, numeric results for two sample Student's *t*-test are shown in the Fig. 6(c): a normal myocardial tissue group (group 1, $n = 5$) and an MI tissue group (group 2, $n = 5$). The difference between the groups was found to be statistically significant ($p < 0.001$) (Fig. 6(c)).

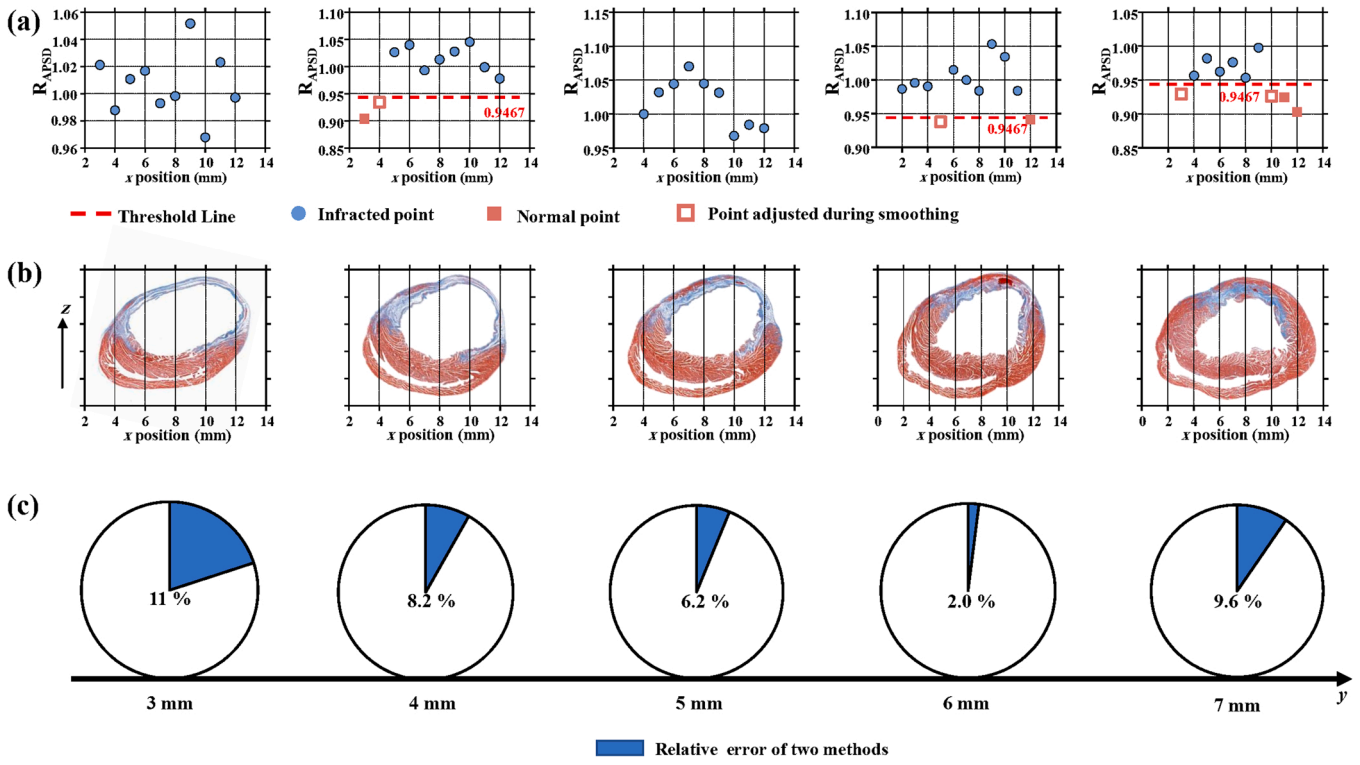

Fig. 7. Typical cross-sectional myocardial infarction (MI) border determination results for each of the five slices of sample number 492. (a) R_{APSD} obtained via DWPASA at different *x* positions for each slice. The blue circles represent R_{APSD} values higher than the threshold and red solid squares represent R_{APSD} values not higher than the threshold. In the smoothing process (as described in Appendix File 2), the groupings of some points are adjusted in line with their connectivity with adjacent points. Thus, some points considered normal before smoothing will be considered infarcted after smoothing, and these points are indicated as hollow squares in the plot. Similarly, about 2% of all points, during smoothing some points originally considered to be infarcted will be transformed into normal points; no examples of these points were seen in the data shown in this figure. For this sample, $R_{threshold} = 0.9467$. (b) Masson staining images of each slice. (c) Relative error between the infarct lengths obtained via the DWPASA and Masson staining methods at different *y* positions.

3.2. Cross-sectional study results

First, we used the DWPASA method to explore the cross sections of the MI border, and the results were compared with standard histological measurements obtained via Masson staining. A typical series of contiguous apex-to-base short-axis cross-sectional results for an MI rat heart (sample 492) is shown in Fig. 7(a) and 7(b). As shown in Fig. 7(a), before smoothing, in the cross sections at the Apex + 3 mm and Apex + 5 mm positions, the DWPASA cumulative length, CL_{DWPASA}, values for the MI border are in good agreement with the corresponding values of the Masson staining cumulative length, CL_M, obtained via histology. (Fig. 7 (b)). After smoothing, in addition to the above-mentioned sections, CL_{DWPASA} values for the cross sections at the Apex + 4 mm, Apex + 6 mm, and Apex + 7 mm positions are quite consistent with those obtained via standard histology. Fig. 7(c) represents the relative error of the infarct length as extracted via DWPASA and standard histology along the *x* axis. The average relative error was less than 7% for five consecutive sections (Sample 492).

To verify the reliability of DWPASA, in comparison with standard histological staining, ten SD rats sacrificed 7 and 14 days after MI (71 tissue slices in total) were studied, and the results are shown in Table A1 (Appendix File 1). The ICCs for the two methods were 0.66 before smoothing, 0.73 after line smoothing, and 0.76 after area smoothing ($p < 0.001$). These correlation results demonstrate the substantial reliability of our DWPASA method for the detection of cross-sectional MI borders. This was also confirmed by a Bland–Altman analysis, from which an absolute mean difference (bias) of 0.05 mm (95% limits of agreements, −2.73 to 2.84 mm) was obtained, as shown in Fig. 8. Table 1.

3.3. Overall MI area border definition

For each sample, we stacked the results for each cross-sectional image as described above to obtain the overall demarcation of the MI area. A typical diagram of the MI area border (sample 492) is shown in Fig. 9. In Fig. 9, the *y* position represents the distance from the apex of the heart and the *x* position represents the distance from the right side of the heart to the point scan position. In Fig. 9(a)–(c), the color of each pixel in the PA border diagrams is determined by the corresponding R_{APSD} value; for a value of R_{APSD} above $R_{threshold}$, the pixel in the PA border diagrams is colored yellow, otherwise, the pixel is colored green. The entire MI area border as determined using the DWPASA method is highlighted by a red solid line for each processing condition (without smoothing, with line smoothing (LS), or with area smoothing (AS), as shown in Fig. 9(a)–(c), respectively).

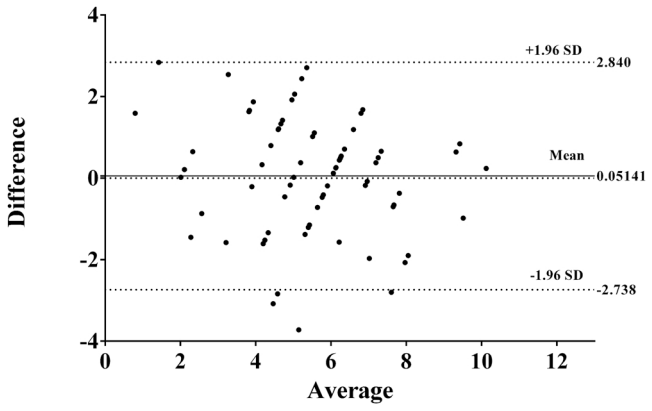

Fig. 8. Bland–Altman plot of difference vs average cross-sectional infarct length ($n = 71$) for DWPASA and Masson staining methods. Legend: central dotted line, mean difference = 0.05 mm; area between upper and lower dashed lines, ± 95% limits of agreement (−2.74 to +2.84 mm).

Table 1
Intra-class correlation coefficients.

	Smoothing		
	None	Line	Area
N	71	71	71
ICC	0.658	0.733	0.755
95% Confidence Interval	[0.406; 0.799]	[0.604; 0.825]	[0.634; 0.840]
P value	< 0.001	< 0.001	< 0.001

N, Slice number; ICC, Intra-class correlation coefficient, two-way random, absolute agreement.

For the border diagrams obtained from the histological results (Fig. 9 (d)), 3D rat hearts were reconstructed from histological tissue slices, and MI zones were rendered on to the reconstructed 3D hearts according to the Masson staining intensities, as described in Section 2.5. The MI area borders demarcated by histological staining are highlighted by a dark blue solid line. The MI area borders obtained via DWPASA and histology are shown together in Fig. 9(e)–(g).

To quantify the agreement between the standard histology results and the DWPASA results, to evaluate the reliability of our new DWPASA modality for the overall MI area border demarcation (in 2D), ten rat MI model hearts were re-examined. Intersection over union (IoU) indexes (detailed in Appendix File 3), which are a measure of the strength of the shape similarities for the borders obtained via the two modalities, were 0.61, 0.69, and 0.72 for DWPASA, DWPASA with line-smoothing, and DWPASA with area-smoothing, respectively, as shown in Fig. 10. A widely reported detection accuracy measure, the mean Average Precision (mAP), for instance in the PASCAL VOC challenge [36], is calculated based on the IoU threshold at 0.5. It may be seen that through smoothing, the lower 95% CI of IoU mean resulted from our study were all greater than the threshold.

4. Discussion

With the current advances in basic cardiovascular research, developing a new imaging system capable of demarcating the MI border is critically important for diagnosis and therapeutic drug delivery [4]. However, conventional imaging systems have limitations. Computed tomography (CT) scanning without a contrast agent is incapable of effectively verifying tissue deformation after MI. MRI provides tissue differentiation, but features the lowest spatial resolution among medical imaging techniques and is very time consuming. Ultrasound provides real-time physical information, such as information on structure and elasticity; however, it is challenging to verify and localize the MI lesion border using ultrasound [20]. The characteristics of emerging PA technique systems are more conducive to meeting the requirements of MI border demarcation. PA technique takes advantage of molecular-information-rich light absorption in biological tissues and minimal sound wave scattering; therefore, the PA technique provides abundant, high-quality imaging data at greater depths (on the order of centimeters) [37]. Pathological changes caused by various diseases modulate PA signals; hence, PA probes can be used to capture and distinguish the changing physical and chemical information, providing biomacromolecular content variations, as well as metabolic state and oxygenation condition variations, including blood perfusion status information in cells, thereby differentiating abnormal tissues from normal tissues.

In this study, we evaluated the feasibility of using DWPASA to demarcate the MI border. Based on the differences between the physiochemical PA spectra of normal and infarcted myocardial tissues, two specific wavelengths, 1310 and 1450 nm, were selected and the R_{APSD} parameter was used to quantify differences in the chemical content of the tissues. The cross-sectional infarct lengths computed from the DWPASA results using our thresholding and smoothing algorithms were in good agreement with corresponding results obtained via standard

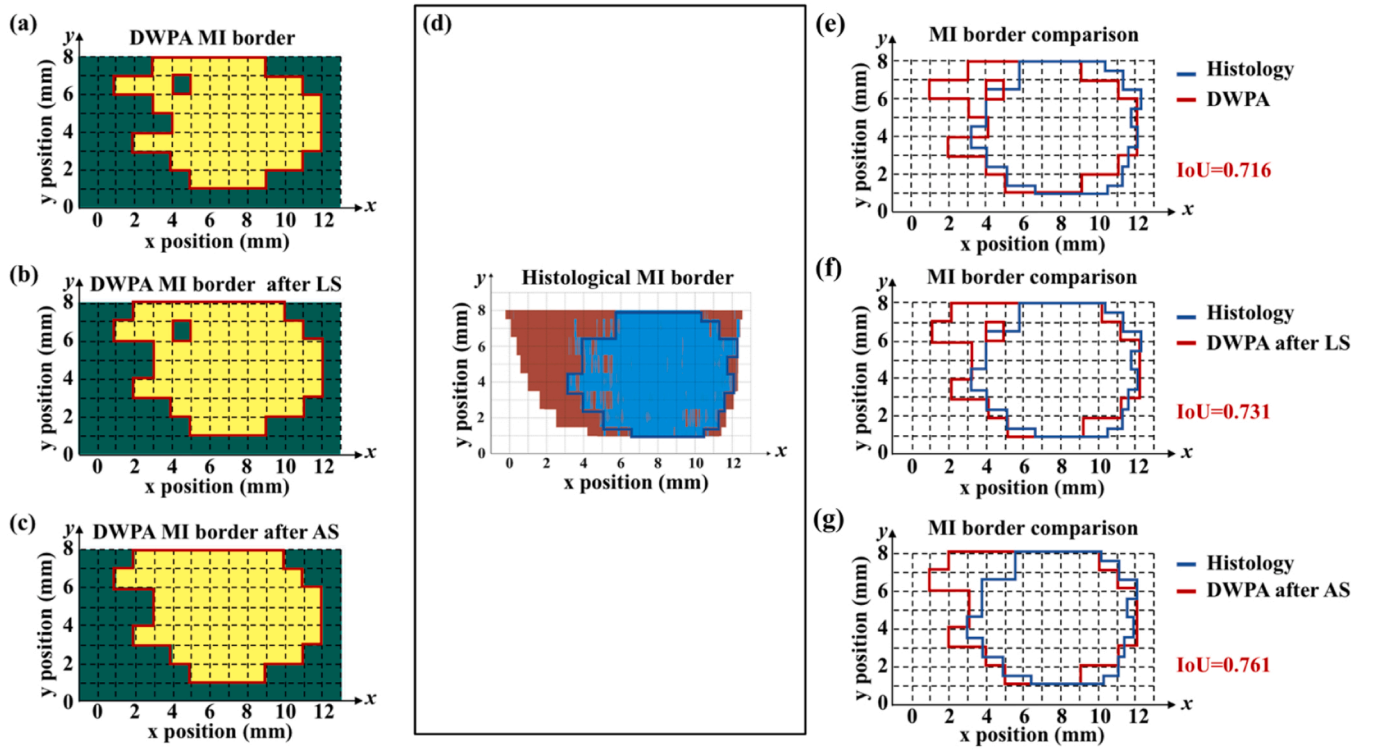

Fig. 9. Typical diagrams showing two-dimensional MI area border (sample number 492). DWPASA overall MI area border demarcation: (a) without smoothing, (b) with line smoothing (LS), and (c) with area smoothing (AS). (d) Schematic of histological MI border. (e)–(g) Schematic diagrams of MI surface as obtained via DWPASA and histological staining.

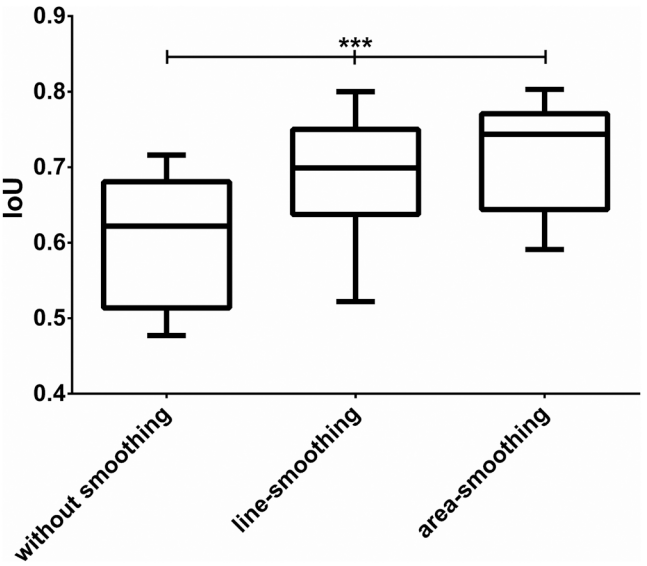

Fig. 10. IoU box plots for the results from ten samples without smoothing and with two smoothing protocols (*** non-parametric statistically significant difference via Friedman's sum of ranks test ($p < 0.001$), Friedman's sum of ranks test was conducted using SPSS software (version 22; IBM Corporation, Armonk, NY)).

Masson staining (ICC = 0.76, 95% CI = 0.634–0.840). Moreover, computed IoU (mean = 0.72, 95% CI = 0.66–0.77) reflected the good agreement at the 2D level between our new PA approach and histological methods of demarcating MI area borders in rat hearts. These ICC and IoU results could be taken as a success for our proof-of-concept study. Compared with Liming Nie et al.'s work [20], our results present a method for automatic MI demarcation with a spatial accuracy approaching the millimeter level which is base of quantitative comparison between affected and unaffected cardiac tissue. By contrast, their work was mainly focused on changes in hemoglobin absorption intensity, and hence the ischemic region was labeled as the infarct region. Moreover, a single-wavelength measurement can only provide relative marker values, and in general this approach fails for the quantification of chemical content variations.

In general, it is well known that MI can cause collagen deposition [21], and hence collagen can be regarded as a molecular biomarker. In the present study, the DWPASA method was used for the first time, to the best of our knowledge, to provide a quantitative and sensitive means of spatially localizing collagen content changes induced by MI. In this approach, the 1310-nm wavelength is used to represent light absorption by collagen molecules as a biomarker of MI tissue and the 1450-nm wavelength represents light absorption by water molecules as a biomarker of normal tissue. Changes in the content of these molecules can reflect the hyperplasia of scar tissue in the infarct areas quantitatively and intuitively. Furthermore, the proposed parameter R_{APSD} defined by Eq. (4) is very sensitive to the relative changes in the two PA biomarkers, and hence it can be used to draw the MI borders more accurately than other PA imaging methods, which are typically based on the extraction of gray values to quantify absorption intensity. Moreover, we showed that by using a threshold and smoothing protocol the MI border can be more accurately demarcated. In the future, we aim to miniaturize and integrate the optical excitation system and PA signal receiver within a fine needle, with the aim of achieving dynamic assessment of chemical and physical information about the heart and developing a new non-invasive border detection method via the observation of chemical changes in vivo.

Despite the abovementioned achievements, it should be mentioned that our study has several limitations. First, it was an *ex vivo* study. To pave the way toward clinical applications, extensive in vivo studies using clinically relevant MI animal models are warranted to obtain a full understanding of the performance and limitations of the DWPASA

approach described in this work. Second, it should be noted that we considered the optical absorptions of single molecules at wavelengths corresponding to their peak optical absorption responses only, and we ignored the absorptions of other molecules at those wavelengths. For example, 1310 nm is the peak absorption wavelength of molecular collagen, but lipids and water also weakly absorb at this wavelength and hence also generate PA signal. Therefore, the actual PA signal includes absorption information for multiple molecules, and hence our future studies will also focus on analyzing the optical absorption spectra of all the chemical components of heart tissue using a spectral fitting procedure to acquire a more precise evaluation of the water and collagen content. Third, to facilitate future clinical application of the method, many aspects of the PA probe design need to be optimized. For example, we used a needle hydrophone to receive the PA signal in this study. However, in a clinical setting, the PA signal receiver might be positioned within the human body, entering via blood vessels, so we need to reduce the size of the PA probe. For in vivo applications, the probe should be miniaturized such that its diameter is no more than 10 F (3 mm), controlled by remote catheter navigation, and delivered into heart chambers via the femoral vessels. Moreover, the wall thickness of the human heart is thicker than that of the rat hearts used in this work, so lower center frequencies for the PA probe also need to be considered in clinical contexts, because of the strong ultrasound attenuation of thick tissue. Despite these limitations, this study successfully proved the feasibility of using DWPASA techniques to assess chemical content alterations in a rat heart MI model and demarcate the MI border.

The unique merits of DWPASA, alongside its target-specific, non-ionizing, and low-cost features, facilitate the accurate evaluation of tissue content as well as oxygenation or metabolism status, which together can provide highly valuable information to aid the study of various cardiovascular diseases. Moreover, in this study, we proved that R_{APSD} is much more sensitive to the disease evolution than PA signal amplitude of individual molecules, and thus can be used as an indicator of disease evolution to distinguish normal and pathological tissues. In the future, we expect that this promising DWPASA modality will be developed into a real-time, minimally invasive, cardiovascular-dedicated endoscopic probe that can be integrated into a clinical platform for diagnostic and therapeutic purposes.

5. Conclusion

In this report, we discussed the feasibility of using DWPASA to demarcate MI borders. By examining the variation in the physiochemical PA spectrograms of normal and MI tissues, two specific wavelengths, 1310 and 1450 nm were selected. Moreover, we introduced the parameter R_{APSD} to quantify the relative amounts of collagen and water in heart tissue. Using thresholding and smoothing methods, our novel DWPASA modality was demonstrated to possess the ability to distinguish MI areas from normal ones. Our experimental results illustrated the merits of applying DWPASA to demarcate MI area borders in rat hearts, with strong agreement with well-established histological methods having been shown. This study provides a promising solution for the development of a minimally invasive, cardiovascular-dedicated endoscopic PA probe with excellent prospects as a potential clinical platform for diagnostic and therapeutic purposes.

Declaration of Competing Interest

The authors declare that they have no known competing financial interests or personal relationships that could have appeared to influence the work reported in this paper.

Data availability

The data that support the findings of this study are available from the corresponding author upon reasonable request.

Acknowledgments

This study was supported by National Natural Science Foundation of China [12034015]; National Key Research and Development Program of China [2017YFC0111400]; Shanghai Municipal Science and Technology Major Project of China [2021SHZDZX0100]; Shanghai Municipal Commission of Science and Technology Project of China [19511132101] and Shanghai Municipal Health Commission of China [20174Y0030].

We would like to thank Editage (www.editage.cn) for English language editing.

Appendix A. Supporting information

Supplementary data associated with this article can be found in the online version at doi:10.1016/j.pacs.2022.100344.

References

[1] L. Yang, Z.R. Gregorich, W. Cai, P. Zhang, B. Young, Y. Gu, J. Zhang, Y. Ge, Quantitative proteomics and immunohistochemistry reveal insights into cellular and molecular processes in the infarct border zone one month after myocardial infarction, J. Proteome Res. 16 (2017) 2101–2112.
[2] A.L. Bui, T.B. Horwich, G.C. Fonarow, Epidemiology and risk profile of heart failure, Nat. Rev. Cardiol. 8 (2011) 30–41.
[3] J. Kang, T.W. Kim, J. Hur, H.S. Kim, Strategy to prime the host and cells to augment therapeutic efficacy of progenitor cells for patients with myocardial infarction, Front. Cardiovasc. Med. 3 (2016) 1–9.
[4] J.M. Duran, S. Taghavi, R.M. Berretta, C.A. Makarewich, T. Sharp, T. Starosta, F. Udeshi, J.C. George, H. Kubo, S.R. Houser, A characterization and targeting of the infarct border zone in a swine model of myocardial infarction, Clin. Transl. Sci. 5 (2012) 416–421.
[5] A. Greco, M. Mancini, S. Gargiulo, M. Gramanzini, P.P. Claudio, A. Brunetti, M. Salvatore, Ultrasound biomicroscopy in small animal research: applications in molecular and preclinical imaging, J. Biomed. Biotechnol. (2012) (2012), https://doi.org/10.1155/2012/519238.
[6] D.J. Brenner, E.J. Hall, Computed tomography — an increasing source of radiation exposure, N. Engl. J. Med. 357 (2007) 2277–2284.
[7] E. Hann, I.A. Popescu, Q. Zhang, R.A. Gonzales, A. Barutçu, S. Neubauer, V. M. Ferreira, S.K. Piechnik, Deep neural network ensemble for on-the-fly quality control-driven segmentation of cardiac MRI T1 mapping, Med. Image Anal. 71 (2021).
[8] J. Yao, A.A. Kaberniuk, L. Li, D.M. Shcherbakova, R. Zhang, L. Wang, G. Li, V. V. Verkhusha, L.V. Wang, Multiscale photoacoustic tomography using reversibly switchable bacterial phytochrome as a near-infrared photochromic probe, Nat. Methods 13 (2015) 67–73.
[9] L. Li, L. Zhu, C. Ma, L. Lin, J. Yao, L. Wang, K. Maslov, R. Zhang, W. Chen, J. Shi, L. V. Wang, Single-impulse panoramic photoacoustic computed tomography of small-animal whole-body dynamics at high spatiotemporal resolution, Nat. Biomed. Eng. 1 (2017).
[10] R.A. Kruger, R.B. Lam, D.R. Reinecke, S.P. Del Rio, R.P. Doyle, Photoacoustic angiography of the breast, Med. Phys. 37 (2010) 6096–6100.
[11] X. Wang, Y. Pang, G. Ku, X. Xie, G. Stoica, L.V. Wang, Noninvasive laser-induced photoacoustic tomography for structural and functional in vivo imaging of the brain, Nat. Biotechnol. 21 (2003) 803–806.
[12] L.V. Wang, S. Hu, Photoacoustic tomography: in vivo imaging from organelles to organs, Sci. (80-.) 335 (2012) 1458–1462.
[13] G. Xu, Z.X. Meng, J.D. Lin, J. Yuan, P.L. Carson, B. Joshi, X. Wang, The functional pitch of an organ: quantification of tissue texture with photoacoustic spectrum analysis, Radiology 271 (2014) 248–254.
[14] T. Feng, J.E. Perosky, K.M. Kozloff, G. Xu, Q. Cheng, S. Du, J. Yuan, C.X. Deng, X. Wang, Characterization of bone microstructure using photoacoustic spectrum analysis, Opt. Express 23 (2015) 25217.
[15] M. Zhang, Y. Chen, W. Xie, S. Wu, J. Liao, Q. Cheng, Photoacoustic power azimuth spectrum for microvascular evaluation, Photoacoustics 22 (2021), 100260.
[16] W. Xie, T. Feng, M. Zhang, J. Li, D. Ta, L. Cheng, Q. Cheng, Wavelet transform-based photoacoustic time-frequency spectral analysis for bone assessment, Photoacoustics 22 (2021), 100259.
[17] S. Wu, Y. Chen, S. Huang, C. Xu, D. Wu, Q. Cheng, Photoacoustic Spectrum Analysis for Quick Identification and Grading of Prostate Cancer, in: 2020 IEEE International Ultrasonics Symposium (IUS), IEEE, Las Vegas, NV, USA, (2020) 1–4.
[18] Yingna Chen, Chengdang Xu, Zhaoyu Zhang, Anqi Zhu, Xixi Xu, Jing Pan, Ying Liu, Denglong Wu, Shengsong Huang, Qian Cheng, Prostate cancer identification via photoacoustic spectroscopy and machine learning, Photoacoustics 23 (2021), 100280.
[19] S. Huang, Y. Qin, Y. Chen, J. Pan, C. Xu, D. Wu, W.Y. Chao, J.T. Wei, S.A. Tomlins, X. Wang, J.B. Fowlkes, P.L. Carson, Q. Cheng, G. Xu, Interstitial assessment of aggressive prostate cancer by physio-chemical photoacoustics: an ex vivo study with intact human prostates, Med. Phys. 45 (2018) 4125–4132.

[20] J. Lv, Y. Peng, S. Li, Z. Guo, Q. Zhao, X. Zhang, L. Nie, Hemispherical photoacoustic imaging of myocardial infarction: in vivo detection and monitoring, Eur. Radiol. 28 (2018) 2176–2183.
[21] C. Humeres, N.G. Frangogiannis, Fibroblasts in the infarcted, remodeling, and failing heart, JACC Basic Transl. Sci. 4 (2019) 449–467.
[22] C. Wood, K. Harutyunyan, D.R. Sampaio, M. Konopleva, R. Bouchard, Photoacoustic-based oxygen saturation assessment of murine femoral bone marrow in a preclinical model of leukemia, Photoacoustics 14 (2019) 31–36.
[23] G. Xu, L.A. Johnson, J. Hu, J.R. Dillman, P.D.R. Higgins, X. Wang, Detecting inflammation and fibrosis in bowel wall with photoacoustic imaging in a Crohn's disease animal model, in: A.A. Oraevsky, L.V. Wang (Eds.), San Francisco, California, United States, 2015: p. 932347. ⟨https://doi.org/10.1117/12.2077634⟩.
[24] G. Xu, Z. Meng, J. Lin, C.X. Deng, P.L. Carson, J.B. Fowlkes, C. Tao, X. Liu, X. Wang, High resolution physio-chemical tissue analysis: towards non-invasive in vivo biopsy, Sci. Rep. 6 (2016) 16937, https://doi.org/10.1038/srep16937.
[25] Yuxiang Ge Ting Feng, Weiya Xie Yejing Xie, Lan Li Chengcheng Liu, Qing Jiang Dean Ta, Qian Cheng, Detection of collagen by multi-wavelength photoacoustic analysis as a biomarker for bone health assessment, Photoacoustics 24 (2021), 100296, https://doi.org/10.1016/j.pacs.2021.100296.
[26] Yejing Xie Ting Feng, Lan Li Weiya Xie, Jing Han Peng Wang, Liming Cheng Dean Ta, Qian Cheng*, Characterization of multi-biomarkers for bone health assessment based on photoacoustic physicochemical analysis method, Photoacoustics 25 (2022), 100320, https://doi.org/10.1016/j.pacs.2021.100320.
[27] S. Huang, D. Lei, Q. Yang, Y. Yang, C. Jiang, H. Shi, B. Qian, Q. Long, W. Chen, Y. Chen, L. Zhu, W. Yang, L. Wang, W. Hai, Q. Zhao, Z. You, X. Ye, A perfusable, multifunctional epicardial device improves cardiac function and tissue repair, Nat. Med. 27 (2021) 480–490.
[28] M. Xu, L.V. Wang, Photoacoustic imaging in biomedicine, Rev. Sci. Instrum. 77 (2006), 041101.
[29] B. Cox, J.G. Laufer, S.R. Arridge, P.C. Beard, Quantitative spectroscopic photoacoustic imaging: a review, J. Biomed. Opt. 17 (2012), 061202.
[30] T. Feng, Y. Zhu, R. Morris, K.M. Kozloff, X. Wang, Functional photoacoustic and ultrasonic assessment of osteoporosis: a clinical feasibility study, BME Front. 2020 (2020) 1–15.
[31] E.F. Juniper, P.M. O'Byrne, G.H. Guyatt, P.J. Ferrie, D.R. King, Development and validation of a questionnaire to measure asthma control, Eur. Respir. J. 14 (4) (2010) 902–907.
[32] J.R. Landis, G.G. Koch, The measurement of observer agreement for categorical data, Biometrics 33 (1977) 159–174.
[33] Y. Zhu, L.A. Johnson, Z. Huang, J.M. Rubin, J. Yuan, H. Lei, J. Ni, X. Wang, P.D. R. Higgins, G. Xu, "Identifying intestinal fibrosis and inflammation by spectroscopic photoacoustic imaging: an animal study in vivo,", Biomed. Opt. Express 9 (4) (2018) 1590.
[34] H.W. Wang, N. Chai, P. Wang, S. Hu, W. Dou, D. Umulis, L.V. Wang, M. Sturek, R. Lucht, J.X. Cheng, Label-free bond-selective imaging by listening to vibrationally excited molecules, Phys. Rev. Lett. 106 (2011).
[35] P. Suranyi, G.A. Elgavish, U.J. Schoepf, B. Ruzsics, P. Kiss, M. van Assen, B. E. Jacobs, B.C. Brott, A. Elgavish, A. Varga-Szemes, Myocardial tissue characterization by combining late gadolinium enhancement imaging and percent edema mapping: a novel T2 map-based MRI method in canine myocardial infarction, Eur. Radiol. Exp. 2 (2018).
[36] M. Everingham, L. Van Gool, C.K.I. Williams, J. Winn, A. Zisserman, M. Everingham, L.K. Van Gool Leuven, B. CKI Williams, J. Winn, A. Zisserman, The pascal visual object classes (VOC) challenge, Int. J. Comput. Vis. 2009 882 88 (2009) 303–338, https://doi.org/10.1007/S11263-009-0275-4.
[37] S. Hu, K. Maslov, V. Tsytsarev, L.V. Wang, Functional transcranial brain imaging by optical-resolution photoacoustic microscopy, J. Biomed. Opt. 14 (2009), 040503, https://doi.org/10.1117/1.3194136.

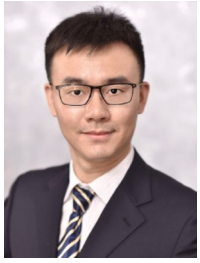

Kangmu Ma received his Ph.D. degree in Neural Science at University of Nebraska Medical Center, Omaha, USA (2013) and MD degree in Cardiovascular Surgery at Shanghai Jiao Tong University School of Medicine, China (2015). In 2013, Kangmu Ma joined the department of cardiovascular surgery in Ruijin Hospital, Shanghai Jiao Tong University School of Medicine. He has been working as an attending cardiovascular surgeon in the heart center of Ruijin Hospital since 2017. His research interests include innovations of minimally-invasive and interventional cardiovascular devices and techniques, as well as novel imaging modalities/processing technologies which are promising for the future diagnosis and treatment of cardiovascular diseases.

Shiying Wu is a Ph.D. candidate student from Institute of Acoustics, School of Physics Science and Engineering of Tongji University. She received Bachelor degree from Tongji University. Her current research focuses on Photoacoustic spectrum analysis and Photoacoustic imaging.

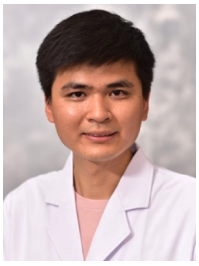

Shixing Huang is currently the resident doctor at Ruijin Hospital, Shanghai Jiaotong University School of Medicine. His work focuses on cardiovascular tissue engineering, stem cells and cardiac repair.

Weiya Xie is a Ph.D. candidate student from Institute of Acoustics, School of Physics Science and Engineering of Tongji University. She received Bachelor degree from Ocean University of China. Her current research focuses on photoacoustic measurement of bone health and photoacoustic imaging.

Mengjiao Zhang is a Ph.D. candidate student from Institute of Acoustics, School of Physics Science and Engineering of Tongji University. She received Bachelor degree from Ocean University of China. Her current research focuses on photoacoustic measurement of microvascular evaluation and photoacoustic imaging.

Yingna Chen is a Ph.D. student in the Institute of Acoustics of School of Physics Science and Engineering at Tongji University at Shanghai, China. Her research interests are in the clinical translation of photoacoustic imaging and spectrum analysis.

Pengxiong Zhu received the MD degree from Shanghai Jiao Tong University in 2018. He is currently the junior attending of Department of Cardiac Surgery, Shanghai East Hospital, Tongji University. His work focused on the basic research and clinical diagnosis and treatment of coronary heart disease.

Jun Liu received the MMed degree from Fudan University in 2001, and the MD degree from Soochow University in 2017. He is currently the vice director of Department of Cardiac Surgery, Shanghai East Hospital, Tongji University. His work focused on the diagnosis and treatment of coronary heart disease and valvular heart disease.

Qian Cheng received the B.S. degree in physics, M.S. and Ph.D. degree in acoustics from Tongji University, China, in 2000, 2003 and 2006, respectively. She is currently a professor at Tongji University. Since 2006, her research interests were optoacoustic phenomena, near-field acoustic imaging technique, Schlieren imaging technique and the development of the acoustic detecting instruments. Her most recent research has focused on the clinical translation of photoacoustic imaging and quantitative analysis.